Fuel 316 (2022) 123250

Contents lists available at ScienceDirect

Fuel

journal homepage: www.elsevier.com/locate/fuel

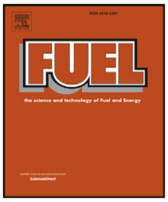

Full length article

CFD modelling of biomass ash deposition under multiple operation conditions using a 2D mass-conserving dynamic mesh approach

Xin Yang [a,*], Hao Zhou [b], Hao Wu [c]

[a] Department of Engineering Science, University of Oxford, Oxford, OX2 0ES, UK
[b] State Key Laboratory of Clean Energy Utilization, Institute for Thermal Power Engineering, Zhejiang University, Hangzhou, 310027, China
[c] Department of Chemical and Biochemical Engineering, Technical University of Denmark, Kgs. Lyngby, 2800, Denmark

ARTICLE INFO

Keywords:
CFD
Biomass
Ash deposition
Dynamic mesh
Ash sticking
Ash erosion

ABSTRACT

A dynamic CFD model with conjugate heat transfer that considers particle sticking and erosion is developed and used for predicting the effect of multiple operation conditions on ash deposition for a model biomass fly ash species ($K_2Si_4O_9$) in a lab-scale entrained flow reactor. In order to achieve stable dynamic mesh morphing, a globally mass-conserving smooth method is proposed using a multiple-point weighted moving average algorithm and a growth scaling factor. A new method to estimate particle count for Lagrangian particle tracking is also proposed, which is based on particle impaction efficiency and face count of the mesh of deposition tube. Particle sticking is predicted based on the two-body collision method and particle erosion is evaluated using the empirical model that is dependent on temperature, particle diameter and velocity, and impaction angle. The proposed smoothing method incorporated with the particle count estimated can accomplish stable dynamic mesh morphing for all the 37 deposition cases without the need to loop the smoothing process and sub-group/averaging the growth rate. The prediction results using the proposed ash deposition model agree reasonably with the experimental observation of the effects of flue gas temperature, tube surface temperature, flue gas velocity, fly ash flux and deposition time on deposit formation rate. R^2 of the predicted and measured deposit formation rates is approximately 0.68. The results also show that the predicted erosion rate essentially correlates negatively with the experimental deposit formation rate. Interestingly, coarse particles are numerically seen to reduce the deposition rate caused by smaller particles via erosion.

1. Introduction

Biomass combustion is regarded as a promising technology to minimize CO_2 emissions in power generations. By integrating with low carbon technologies (oxy-fuel and chemical looping) and carbon capture technologies, there is a potential to achieve net negative CO_2 emissions for biomass combustion [1]. In 2020, China announced to fulfil the target of carbon neutrality in the year 2060. Nowadays, nearly 70% of the energy-related CO_2 emissions are from coal in China [2]. Therefore, biomass utilization could be an effective way to reduce coal consumption and carbon emission in China. However, due to the inorganic content in biomass (potassium, chlorine, etc.) [3,4], biomass combustion systems often confront with ash related issues, including slagging, fouling and corrosion. These problems cannot only reduce the thermal efficiency of a boiler, but also lower boiler availability. Therefore, being able to understand and predict ash deposit formation are important for the design and operation of biomass combustion systems.

CFD methods have been widely used for predicting ash deposition behaviours in biomass combustion (for understanding sticking behaviours of coarse molten alkali-rich fly ashes [5], for fine and coarse particle deposition in straw-fired boilers through empirical correlated inertial impaction, thermophoresis and turbulent impaction [6], for KCl evaporation/condensation and fine particle deposition in small scale biomass boilers [7,8]). Ash deposition on a heat exchanger tube is a dynamic process. Deposit formation affects dynamically the flowfield near the tube, which can result in the change of the contribution of particle deposition mechanisms and particle net sticking behaviours [9]. Up to now, only a limited number of studies have investigated ash deposition through a CFD simulation using dynamic mesh morphing and incorporating the influence of heat transfer to the tube. García Pérez et al. [10] modelled the fouling growth of fume ash particles on 2D tube banks of kraft recovery boiler using dynamic meshes. A multiple iterative growth smoothing method, which is based on a multiple-point weighted moving average algorithm, was proposed in order to resolve

---

[*] Corresponding author.
E-mail address: xin.yang@eng.ox.ac.uk (X. Yang).

https://doi.org/10.1016/j.fuel.2022.123250
Received 22 September 2021; Received in revised form 30 December 2021; Accepted 9 January 2022

Nomenclature

$A_{arrival}$	mass flux of the arrival ash particles at deposition surface (kg m^{-2} s^{-1})
A_{inlet}	ash mass flux (kg m^{-2} s^{-1})
A_n	growth area of a face grid (m^2)
A_t	total growth area (m^2)
D_p	particle diameter (m)
E	Young's modulus (Pa)
$Ex_E^{\star}$	excess energy (–)
$\overrightarrow{f_n}$	normal direction vector of a face grid (–)
F_{scale}	growth scaling factor (–)
K	heat conductivity (W m^{-1} K^{-1})
IE_f	particle impaction efficiency on a face grid (–)
IE_t	mean particle impaction efficiency on the deposition surface (–)
MAD	mean absolute difference (–)
N_p	particle count (–)
R_{dep}	ash deposition rate (kg m^{-2} s^{-1})
$\overrightarrow{r_n}$	node coordinate vector (–)
H and H_{cr}	deposit heigh and critical deposit height (m)
T	temperature (K)
V_g	flue gas velocity (m s^{-1})
V_I	particle impaction velocity magnitude (m s^{-1})
V_{cr}	critical normal impaction velocity (m s^{-1})
δ_f	thickness growth on a face grid (m)
δ_{node}	thickness growth on a node grid (m)
η_{dep}	deposition efficiency (–)
η_e	erosion efficiency (–)
η_s	sticking efficiency (–)
θ_{cr}	critical particle impaction angle (°)
θ_I	particle impaction angle (°)
ρ_p	particle density (kg m^{-3})
ϕ	deposit porosity (–)

Subscript

g	gas
p	particle
$surf$	deposit surface
t	tube surface

the issue of mesh instabilities and model crashes. It was observed that the sub-micron particles of 0.7 μm showed a uniform deposition by thermophoresis while the particles of 3.62 μm showed a more irregular deposition. Tang et al. [11] investigated the effect of geometry and arrangement of heat exchanger tube bundles on the fouling of fly ash particles. A multiple mean cycle method was developed in order to resolve the mesh issue similar to that of García Pérez et al. [10]. It was seen that the staggered elliptical tube bundle can reduce both fouling and heat transfer abatement comparing with the aligned circular tube bundle [11]. The numerical results of Mu et al. [12] using a dynamic ash deposition model also suggest an optimal shape and arrangement of tube bundles for reducing ash deposition. Zheng et al. [13] studied the ash deposit growth on a single heat exchanger tube in a pilot-scale furnace using dynamic mesh morphing. In order to achieve stable dynamic mesh morphing, the authors divided the grid faces of deposit surface into sub-groups with an assumption of uniform growth in each group and then redistributed the growth of each face group using a weighting factor. A similar smoothing strategy was used in the dynamic ash deposition model by Zhou et al. [14].

In addition to the development of dynamic mesh morphing techniques for ash deposition model, a few studies investigated the effect of particle removal/erosion behaviour on overall ash deposit formation. Strandström et al. [15] developed the first velocity-dependent particle erosion model for ash deposition in an entrained flow reactor. The erosion model was evaluated by comparing particle impact energy and work of adhesion of deposit. It was observed that sand particles were able to clean deposits. Liu et al. [16] modelled the ash deposition of a high-alkali coal in a large-scale furnace. A particle erosion model, which was based on evaluating the ratio of particle excess energy to surface energy of deposit, was proposed. It was seen that the predicted ash deposit mass with particle erosion was much closer to the experimental data than that without particle erosion. A similar particle erosion model was recently proposed by Zhou et al. [17] to model ash deposition in a pilot-scale furnace. In addition to these energy-based particle erosion models, a moment-based particle erosion model was used in the ash deposition models by Tang et al. [11] and Zheng et al. [18]. It was observed that the deposit mass reduced by 24% with the flue gas velocity of 1.93 m/s in a lab-scale entrained flow reactor and therefore the authors suggested to consider particle removal/erosion behaviour in order to better predict ash deposition [18].

These ash deposition models have improved the understanding and prediction of ash deposition. However, the deposit growth after smoothing may not be mass-conservative. In these dynamic ash deposition models, it is also unclear how to determine particle count which is a significant factor in dictating the independence of particle tracking solution and affecting dynamic mesh morphing. Furthermore, there is limited CFD-based ash deposition modelling work that has been compared against tests covering multiple operation conditions simultaneously (temperature, velocity, deposition time, etc.). Therefore, this study aims to develop (i) a mass-conserving smooth method using particle count which is dependent on mesh size and particle impaction efficiency and (ii) a dynamic ash deposition model with conjugate heat transfer that can predict the effects of multiple operation conditions. In a conjugate simulation, the solid zone, which is composed of tube metal and deposit layer, is meshed and the energy equation is solver on both solid and fluid meshes. This improves the prediction performance of thermal impact of deposition. The ash deposition experiments of a model biomass ash species ($K_2Si_4O_9$) in a lab-scale entrained flow reactor carried out by Laxminarayan et al. [19] are used. The effects of flue gas temperature (T_g), flue gas velocity (V_g), tube surface temperature (T_t), deposition time and ash flux (F_{par}) on deposit formation rate were studied in the experiments. The two-body collision method described by van Beek [20] is employed to predict particle sticking/rebound behaviour. The empirical particle erosion model recently proposed by Libertowski et al. [21], which is based on the erosion tests by injecting non-sticky dust particle onto a deposited surface, is employed. In order to take into account the effect of temperature on ash deposition, Young's modulus is assumed to be temperature dependent in the particle sticking model and the empirical erosion model is extended via adding terms of deposit surface temperature and particle temperature.

2. Source of experimental data

Ash deposition experiments were conducted in a lab-scale entrained flow reactor (EFR). The purpose of the experiments was to improve the understanding of biomass fly ash deposition, as well as providing a database for the validation of ash deposition models under well defined conditions. The EFR setup consisted of a gas supply system, a screw feeder, a gas preheater, a electrically heated furnace with an inner diameter of 80 mm and a length of 2 m, and a bottom chamber with a deposition probe system [19]. The schematic diagram of the EFR setup is shown in Appendix A. Ash particles were fed into the furnace together with primary air, as well as preheated secondary air. $K_2Si_4O_9$

particles were used as the model biomass fly ash species. This is because fly ashes and deposits of biomass, especially herbaceous biomass, contain significant quantities of amorphous silicates, characterized by their viscoelastic behaviour [19,22–24]. Compared with studies dealing with ash deposition in combustion systems [25,26], using $K_2Si_4O_9$ particles gets rid of the need to simulate combustion and fly ash formation. This decreases the complexity and numerical uncertainty in a CFD-based ash deposition model [27]. After travelling through the furnace, the gas and particles entered the bottom chamber where the cooled stainless steel ash deposition probe was placed. The probe, which was mounted on a retractable annular air cooling probe, has an outer diameter of 10 mm and a thickness of 1 mm. The dimension is much smaller than that of a real superheater tube in order to better match particle Stokes number of the lab-scale reactor with that in boilers. The temperature, which was measured between the inner surface of the steel tube and the outer surface of the cooling tube, is assumed to be the inner surface temperature of the steel tube (referred to as tube surface temperature). The temperature was electronically controlled during ash deposition tests. The flue gas temperature was measured at the bottom chamber using a suction pyrometer. The deposit formation rate was characterized by the ratio of the deposit mass to the particle feeding time (referred to as deposition time) and the outer surface area of the steel probe exposed to flue gas [22].

Multiple operation conditions were tested at varied flue gas temperature ranged from 589 to 968 °C, tube surface temperature ranged from 300 to 550 °C, gas velocity ranged from 0.7 to 3.5 m/s, deposition time ranged from 7.5 min to 60 min, and fly ash flux ranged from 1×10^4 to 4×10^4 $g/(m^2\ h)$, as shown in Appendix B. The flow Reynolds number based on the inner diameter of the reactor and the outer diameter of the steel probe, Re_r and Re_p, are in the ranges from 4.4×10^2 to 1.87×10^3 and 55 to 2.34×10^2, respectively. The ash particle Dv_{10}, Dv_{50} and Dv_{90} are 7.31, 62.3 and 272 μm, which were from dry particle size measurement using a Malvern Mastersizer 3000, as shown in Appendix C. The measured size distribution is used in modelling the ash deposit formation [25]. Fume particle size (i.e., submicron size) is not used in order to reduce the complexity of ash deposition mechanisms and focus on inertial impaction, as well as thermophoresis. The experimental uncertainty was characterized by the relative standard error of 4% based on 5 repetitions of the baseline experiments.

3. Mathematical models

3.1. Ash deposition model

Ash deposition model describes the models used to predict ash deposition rate and its interaction with the thermal condition at the deposit layer formed on the steel tube. To achieve this, several submodels have been developed and applied in the CFD framework. In this section, the sticking model of the particles and the deposition surface is introduced, followed by a description on the particle erosion model, as well as the heat conduction in the deposit layer.

As mentioned in the section of Introduction, both particle sticking and erosion are taken into account in the deposit formation. Therefore, ash deposition rate on a grid face of the tube, R_{dep}, may be predicted by:

$$R_{dep} = \max(A_{arrival}\eta_s - A_{arrival}(1-\eta_s)\eta_e, 0) \tag{1}$$

where $A_{arrival}$ is the mass flux of the arrival ash particles at deposition surface predicted from particle tracking using the discrete phase model (DPM) in Ansys Fluent; η_s is the sticking efficiency; η_e is the erosion efficiency. In this study, inertial impaction and thermophoretic force are assumed to be the main mechanisms of particle transportation. Condensation is not considered for the $K_2Si_4O_9$ particles. Turbulent dispersion of particles is neglected due to the low flow Reynolds number of the lab-scale reactor (Re_r in the range from 4.4×10^2 to 1.87×10^3). For a full-scale boiler, the turbulent dispersion needs to be considered using either the random walk model [28] or large eddy simulation [29]. The probe Reynolds number, Re_p, which ranges from 55 to 2.34×10^2, is above the critical value, 48, to trigger unsteady vortex shedding [30]. The unsteady flow behaviour may lead to ash deposition of fine particles at the leeward section of deposition tubes [10]. However, due to that the particles (Dv_{50}=62.3 μm) are relatively coarse, vortex shedding is neglected in this study. This assumption is validated against the experimental observation that there was no deposit formation at the leeward section of the deposition probe.

3.1.1. Sticking

Particle sticking and rebounding behaviours are dictated by particle chemistry, particle physical properties, and deposit surface properties. Due to that the flue gas temperature investigated covers temperatures below hemispherical temperature of $K_2Si_4O_9$ (852 °C [31]), the approach of two body collision by van Beek [20] is used to predict the sticking efficiency and particle rebound velocities. This approach has been used by other researchers to model ash deposition at furnace temperatures below ash fusion temperature [10,11,18]. In order to extend the approach for the conditions of varied flue gas temperatures, the Natural logarithm of Young's modulus (E) of $K_2Si_4O_9$ particles and deposit surface is assumed to be linearly correlated with temperature. This assumption is similar to the assumption implemented by Ai et al. [32]:

$$E = A_0 e^{(B_0 T)} \tag{2}$$

where A_0 and B_0 are the coefficients of the correlation, $= 9.74 \times 10^{10}$ and -1.155×10^{-2} respectively, which are derived from fitting the training data of the ash deposition tests. 8 sets of test data, which cover the baseline test (Test No. 4) and the other 7 tests at the upper and lower bounds of each operation conditions, are selected as the training data.[1] Correspondingly, the training data accounts for 22% of all the test data. T is the temperature of impact particles and deposit surfaces. The process to implement the two body collision model mainly includes: (i) determining the critical particle impaction angle, θ_{cr}, which is the highest angle that an impact particle is possible to stick [33]; (ii) determining whether the impact contains elastic deformation alone or contains both elastic and plastic deformation based on the critical normal impaction velocity, V_{cr}; (iii) analysing the excess energy ($Ex_E^\star$) based on the energy conservation analysis during particle impaction; and (iv) predicting the sticking efficiency (η_s) and particle rebound velocities (V_{rn} and V_{rt}). If particle impaction angle[2] (θ_I) $< \theta_{cr}$ and $Ex_E^\star \le 0$, particle will stick ($\eta_s = 1$), otherwise particle will rebound. The detailed equations to implement the model can be found in Appendix C. Here, the method related to the initial deposit surface condition is introduced. At the initial stage of ash deposition, the steel surface may be only partially covered with deposits. Therefore, particles may impact on a deposition surface or a clean steel surface. This indicates that a method to distinguish between these two scenarios should be added. The critical minimal thickness (H_{cr}) of a local tube surface being fully covered with deposits may be related to that when the surface is fully covered by a layer of single particles. Therefore, it maybe assumed that: (i) H_{cr} equals to the mean particle size; (ii) If a local thickness, H, is below H_{cr}, the probability of particles to impact on the deposited part of a local deposit surface, P_{dep}, equals to the ratio of H to H_{cr}; (iii) If H is higher than H_{cr}, particles impact on a fully deposited local surface:

$$P_{dep} = \begin{cases} \frac{H}{H_{cr}} & H < H_{cr} \\ 1 & H \ge H_{cr} \end{cases} \tag{3}$$

---

[1] Note: The tests used as the training data are marked in the table presented at Appendix B.

[2] Note: Particle impaction angle equals to arctan operation of the ratio of particle tangential velocity to particle normal velocity.

$$\eta_s = P_{dep}\eta_{s,dep} + (1 - P_{dep})\eta_{s,steel} \tag{4}$$

where $\eta_{s,dep}$ and $\eta_{s,steel}$ are the sticking efficiency evaluated using the effective Young's modulus ($E^{\star}$) based on the Young's modulus of local tube surface (E_{surf}) of deposit and steel respectively.

3.1.2. Erosion

Ash deposition may be removed from the surface by the erosion of impinging ash particles. Recently, Libertowski et al. [21] experimentally studied the erosion behaviour of dust ash particles on a deposited surface. It was observed that the erosion rate increased with particle diameter and velocity and decreased with increasing temperature. They proposed an empirical erosion model, which is a function of particle diameter (D_p), velocity (V_I) and impaction angle (θ_I). The erosion model was implemented in their CFD models and the prediction results in the deposition profile after erosion matched well with the experimental observation. Therefore, in this study, the empirical erosion model by Libertowski et al. [21] is employed. It is assumed that erosion rate reduces with the increase in deposit surface temperature (T_{surf}) and particle temperature (T_p). This is because that: (i) the sintering degree of deposit increases with the temperature and (ii) particles with higher temperature may be less hard to erode the deposition. Therefore, the extended empirical erosion model may be expressed by:

$$\eta_e = C_0 \sin^2\left(\frac{\pi}{2} - \theta_I\right)\left(\frac{V_I}{V_{ref}}\right)^{D_0}\left(\frac{D_p}{D_{ref}}\right)^{1.2}\left(1 + \frac{T_{ref,1}}{T_{surf}}\right)^{E_0}\left(1 + \frac{T_{ref,2}}{T_p}\right)^{F_0} \tag{5}$$

where C_0, D_0, E_0 and F_0 are the coefficients of the correlation, = 6.21×10^{-7}, 0.5, 3.84 and 4 respectively, which are derived from fitting of the training data presented in Appendix B; V_{ref} and D_{ref} are the values of the reference velocity and temperature = 1 m/s and 1×10^{-6} *m* [21]; $T_{ref,1}$ is the reference temperature = 748.15 *K*, which is the tube surface temperature of the baseline test; $T_{ref,2}$ is the reference temperature = 1054.15 *K*, which is the flue gas temperature of the baseline test.

3.1.3. Heat conduction in deposit layer

Deposit surface temperature affects both particle sticking and erosion behaviour. Hence, mesh morphing is used in a conjugate heat transfer. A solid zone, which is composed of deposit layer and the steel tube, is created in the CFD computational domain. Heat conduction in the deposit layer is directly resolved using the CFD solver. The deposit layer is assumed to be porous with a constant porosity (ϕ) of 0.6 [6,34]. The liquid phase dependent porosity is not considered as the deposit surface temperatures for most cases are below the deformation temperature and hemispherical temperature of $K_2Si_4O_9$ (710 and 852 °C). In addition, a further analysis using the liquid phase dependent porosity model presented by Richards et al. [34] indicates that the difference in the predicted deposit formation rate between the constant porosity and liquid phase dependent porosity is small. More details can be found in Appendix F. The thermal conductivity of the deposit layer, k_{dep} is predicted using the method proposed by Sugawara and Yoshizawa [35]:

$$F = \frac{2^n}{(2^2 - 1)}\left(1 - \frac{1}{(1+\phi)^n}\right) \tag{6}$$

$$k_{dep} = (1 - F)k_p + Fk_g \tag{7}$$

where n is the empirical parameter = 6.5, k_p and k_g are the thermal conductivities of $K_2Si_4O_9$ particles and air respectively, which are functions of temperature. More details of the material properties used can be found in Appendix E.

3.2. Ash deposit growth

Ash deposit growth changes the interface of solid zone and fluid zone, which is updated according to the local thickness growth of ash deposition. The thickness growth on a grid face at a time step, δ_f, is defined by:

$$\delta_f = \frac{R_{dep}}{\rho_p(1-\phi)}\Delta t \tag{8}$$

where Δt is the time step size. Due to the discrete nature of Lagrangian particle tracking method, the predicted δ_f maybe un-smoothly distributed on the wall surface, especially when the particle count tracked is not large enough. This can gradually lead to unphysical ash deposit growth and it may even cause the crush of dynamic mesh morphing [10]. Therefore, a smoothing method may be required to re-distribute the local thickness growth. The multiple-point weighted moving average algorithm is used to smooth the growth, which is expressed by:

$$\delta_{f,ns} = \frac{1}{\left(\frac{(k_s+1)}{2}\right)}\delta_{f,n} + \sum_{i=1}^{(k_s-1)/2}\frac{i}{\left(\frac{(k_s+1)}{2}\right)^2}\left(\delta_{f,\left(n-\frac{(k_s+1)}{2}+i\right)} + \delta_{f,\left(n+\frac{(k_s+1)}{2}-i\right)}\right) \tag{9}$$

where $\delta_{f,ns}$ is the local thickness growth after smoothing, n is the index of local face; k_s, which is an odd, is the number of physically adjacent faces used in the smoothing. In this study, k_s=5.[3] In order to obtain the physically adjacent faces for the smoothing method, an order list is generated to get the index list of the physical face connectivity and looping face connectivity of wall faces in the parallel Ansys Fluent based face-looping macro, as shown in Fig. 1.

After the thickness growth is smoothed, the node thickness growth, $\delta_{node,n}$ is averaged by the two adjacent faces:

$$\delta_{node,n} = \frac{1}{2}(\delta_{f,ns} + \delta_{f,n_i s}) \tag{10}$$

where n and n_i are the index of a pair of faces connected to the n node. The coordinate update of the node is derived from the node thickness growth, $\delta_{node,n}$, and the unit mean normal direction vector of the pair of faces, $\overrightarrow{f_{n,m}}$:

$$\overrightarrow{f_{n,m}} = \frac{\overrightarrow{f_n} + \overrightarrow{f_{n_i}}}{|\overrightarrow{f_n} + \overrightarrow{f_{n_i}}|} \tag{11}$$

$$\overrightarrow{r'_n} = \overrightarrow{r_n} + \delta_{node,n}\overrightarrow{f_{n,m}} \tag{12}$$

where $\overrightarrow{r'_n}$ and $\overrightarrow{r_n}$ are the updated and original node coordinates respectively.

Deposit growth after smoothing may be not mass-conservative. Therefore, a growth scaling factor, F_{scale}, which is defined by the ratio of the original growth area without smoothing (A_t) to total growth area after smoothing ($A_{t,s}$), is used to scale the node growth in order to achieve globally mass-conservative deposit growth:

$$F_{scale} = \frac{A_t}{A_{t,s}} \tag{13}$$

$$\delta_{node,ns} = F_{scale}\delta_{node,n} \tag{14}$$

where $\delta_{node,ns}$ is the node thickness growth after considering mass-conservation and it is used to update node coordinates at the interface. $A_{t,s}$ and A_t are obtained by summing up the growth area of all the local faces of the deposit tube. The growth area of a local face, = $|A_n|$, is

---

[3] Note: In this study, using k_s=5 can achieve stable dynamic mesh morphing for all the 37 cases investigated. Either the multiple looping of the smoothing process [10,11] or the process of sub-grouping grid faces and averaging the growth of these sub-grouped faces [13,14], which increases the smooth degree, is not required in this study. When k_s=5, $\delta_{f,ns} = \frac{3}{9}\delta_{f,n} + \frac{1}{9}(\delta_{f,n-2} + \delta_{f,n+2}) + \frac{2}{9}(\delta_{f,n-1} + \delta_{f,n+1})$ according to Eq. (9).

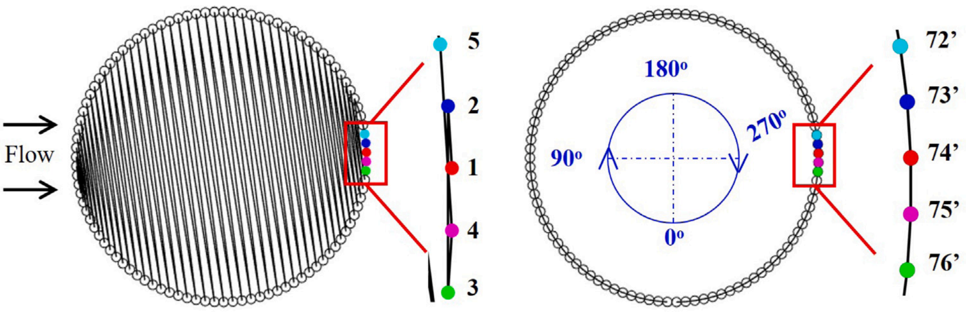

Face connectivity in the face looping marco   Physical face connectivity in clockwise direction

Fig. 1. An example of the looping face connectivity and physical face connectivity of the grid faces at the interface.

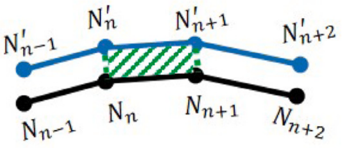

Fig. 2. The growth area of a local face composed of the four nodes, N_n, N_{n+1}, N'_{n+1} and N'_n.

derived from the coordinates of the four nodes as shown in Fig. 2:

$$\begin{aligned}2A_n = &\left(\overrightarrow{r_n[0]}\overrightarrow{r_{n+1}[1]} - \overrightarrow{r_n[1]}\overrightarrow{r_{n+1}[0]}\right) + \left(\overrightarrow{r_{n+1}[0]}\overrightarrow{r'_{n+1}[1]} - \overrightarrow{r_{n+1}[1]}\overrightarrow{r'_{n+1}[0]}\right)\\ &+ \left(\overrightarrow{r'_{n+1}[0]}\overrightarrow{r'_n[1]} - \overrightarrow{r'_{n+1}[1]}\overrightarrow{r'_n[0]}\right) + \left(\overrightarrow{r'_n[0]}\overrightarrow{r_n[1]} - \overrightarrow{r'_n[1]}\overrightarrow{r_n[0]}\right)\end{aligned} \tag{15}$$

where n and $n+1$ are the node index; the superscript symbol, $'$, represents the node after deposit growth as shown in Fig. 2; $\overrightarrow{r[0]}$ and $\overrightarrow{r[1]}$ are the x and y coordinates for a two dimensional case respectively.

3.3. Integration of ash deposition model into the CFD framework

The particle laden flow is modelled via Euler–Lagrange approach using Ansys Fluent 19.2. Mathematical submodels, such as the realizable $\kappa-\epsilon$ viscous model with enhanced wall treatment,[4] Discrete Ordinate model and Discrete Phase Model (DPM), are used for modelling the aerodynamic flow, radiation heat transfer and particle trajectories. The present CFD model focuses on the flow region around the deposition tube being placed at the bottom of the reactor. The computational domain is a 2D geometry with the clean steel tube of diameter 10 mm placed in the central region. Fig. 3 shows a schematic diagram of the computational domain and the meshing scheme around the deposition tube. In this paper, all the 37 cases mentioned in Appendix B have been investigated. The boundary conditions (including inlet temperature and velocity, tube surface temperature, and ash mass flux) use the values presented in Appendix B. The ash particles, which are based on a Rosin–Rammler distribution of 0.844 spread number and 98.3 μm mean diameter and 50 intervals, are assumed to be uniformly distributed at the inlet and are injected at the 15 mm central region in order to reduce the particle count required. The velocity and temperature of ash particles at the inlet are assumed to equal to those of the flow. As shown in Fig. 3, an unstructured mesh is used and the computational domain is composed of solid zone and fluid zone. At the beginning of ash deposition, the solid zone is the clean steel tube with a thickness of 1 mm and the tube outer surface is the fluid–solid interface. During ash deposition, the solid zone is composed of the steel tube and deposit layer and the deposit outer surface is the fluid–solid interface. Quad meshes are generated at both sides of the interface in order to accurately predict particle behaviours near the boundary and resolve the heat conduction in the solid layer. The size of the quad meshes around the interface at the fluid side is approximately 0.05 mm in the direction normal to interface, which is suggested by [36] while a smaller size is used at the solid side as this does not greatly increase the cell count in the solid zone. Dynamic mesh morphing is achieved using: (i) the spring based smoothing and remeshing methods in the Ansys Fluent to update the fluid and solid zones; (ii) the user-defined-function ‘DEFINE_GRID_MOTION’ to update the node coordinates at the interface. In the smoothing method, the spring constant factor, which is used to control the damping of node displacement, is 0.1. In the remeshing method, the minimum and maximum cell size thresholds for the solid zone, which are used to update local too large and small cells, are 9×10^{-5} m and 2.2×10^{-4} m respectively, which are based on the min and max cell size in the solid zone of the initial mesh. All other settings in the smoothing and remeshing methods are set as default. Fig. 4 shows a brief flow chart of the algorithm used to carry out the quasi-transient calculation of the dynamic ash deposition process. In a time step, flowfield in the fluid zone and heat conduction in the solid zone are resolved. Particle tracking and particle sticking/erosion are performed to predict ash deposition rate. The coordinates of the nodes at the interface are then calculated. The mesh is dynamically updated at the end of the time step. In the next time step, CFD calculation, particle tracking, calculating deposit formation rate, interface/mesh updating are continued based on the updated mesh in the previous time step. The calculation ends when time reaches the deposition time for each case.

A numerical independence study, which is needed to understand the computational accuracy and time to be balanced, is carried out at three levels: (i) the particle count, N_p, which is the number of particles injected into the domain, (ii) the mesh, and (iii) the time step size, Δt. In this study, an approach is proposed to estimate N_p. In order to consider the discrete nature in the Lagrangian particle tracking method, N_p should be related to the particle impaction efficiency and the face count of the fluid–solid interface and it may be expressed by:

$$N_p = N_{intv}\frac{L_{inj}}{L_{proj}}\frac{1}{IE_t}\frac{N_f}{K_A} \tag{16}$$

$$IE_t = \frac{K_A A_{arrival,m}}{A_{inlet}} \tag{17}$$

where N_{intv} is the interval of particle size distribution, = 50; L_{inj} is the length of the injection location, = 15 mm; L_{proj} is the projected length of the clean deposition tube, = 10 mm; IE_t is the mean impaction efficiency of particles on the tube; N_f is the number of grid face on the

---

[4] Note: Realizable $\kappa-\epsilon$ viscous model is used due to its popularity and accuracy. The effect of turbulence models (including standard $\kappa-\epsilon$ and SST κ -ω) is marginal for the cases investigated in this study.

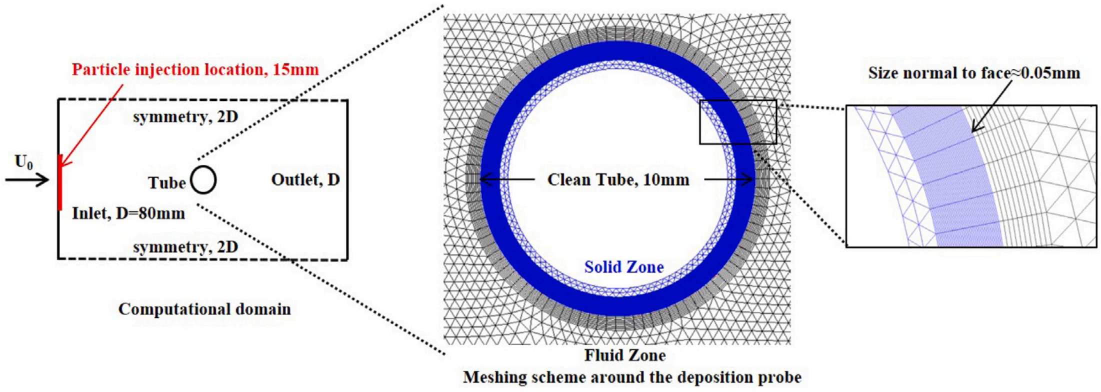

Fig. 3. Schematic diagram of computational domain and meshing scheme around the deposition tube.

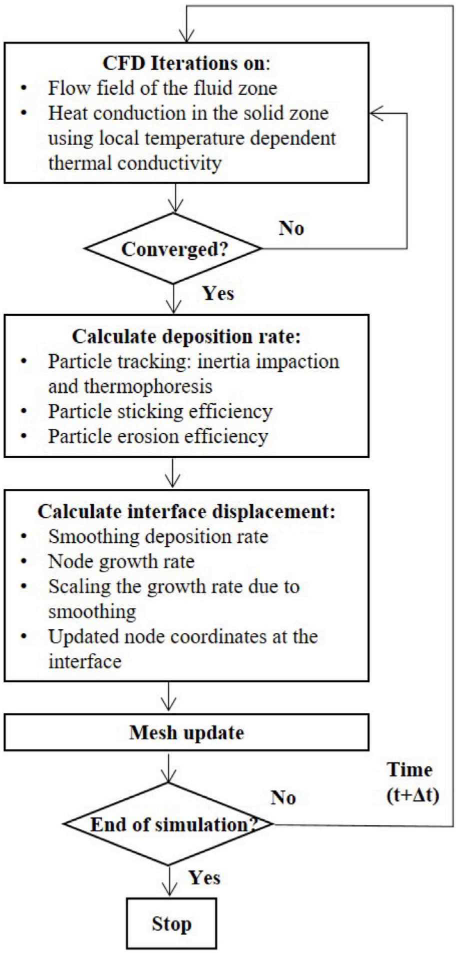

Fig. 4. The algorithm of the dynamic ash deposition model integrated with the CFD framework.

tube, = 100; $A_{arrival,m}$ is the mean mass flux of the arrival ash particles at the clean tube surface; A_{inlet} is the ash mass flux at the inlet; K_A is the deposition factor, = 2 as deposit formation only occurs at the windward section of the tube.[5] IE_f, which is the particle impaction efficiency at a grid face, is a important indicator of the severity of ash deposition and sensitive to particle count and mesh. Therefore, it is used as the parameter for comparing the results of independent studies of particle count and mesh. The change in IE_f between cases is measured using mean absolute difference (MAD) of IE_f. IE_f and MAD are defined by:

$$IE_f = \frac{A_{arrival}}{A_{inlet}} \tag{18}$$

$$MAD = \left(\sum_{i=1}^{n}\left|IE_{f_i,X} - IE_{f_i,Y}\right|\right)/n \tag{19}$$

where $IE_{f_i,X}$ is the impaction efficiency at the test setting (of Np or mesh); $IE_{f_i,Y}$ is the impaction efficiency at the finest setting (of Np or mesh) conducted in the independence study.

The independence study was carried out for the baseline case on a clean tube. Fig. 5 shows IE_f using five different particle counts. It is observed that increasing particle count from $0.125N_p$ to $2N_p$ lead to smoother profile of particle impaction efficiency and the MAD reduces from 3.0% to 0.6% with increasing the particle count from $0.125N_p$ to N_p. This indicates that the particle count estimated using the proposed approach is suitable to estimate the particle count required for the cases investigated. Fig. 6 shows IE_f using three different meshes, including coarse mesh with 2×10^4 cells and 50 faces on the interface, medium mesh with approximately 8×10^4 cells and 100 faces on the interface, and fine mesh with approximately 33×10^4 cells and 200 faces on the interface. The medium mesh yields results close to that of the fine mesh, as shown in Fig. 6 and hence the medium mesh is used. The MAD is 0.8%. Δt, which is set to be small at the initial stage and large at the later stage, is initially set to be 10 s in the first 3 min and 30 s in the rest time. In the independence study, the smaller Δt is set to be one fourth of the values initially given. There is little difference in both the deposit profile and total deposit mass. Therefore, the initial values of Δt are used in the simulation.

4. Results and discussions

4.1. The baseline cases (T_g=781 °C, T_t=475 °C, V_g = 1 m/s and F_{par}=20 400 g/(m^2 h))

4.1.1. Heat transfer

Fig. 6 shows the temperature contour of the solid zone, heat flux and temperature of the deposition surface for deposition time of 0, 15 and 60 min. As mentioned in the subsection of ash deposition model, heat conduction in the solid zone (composed of deposit and metal tube) is resolved based on the temperature dependent thermal conductivity of deposits. Due to the increase in the thickness of deposit layer, which has a relatively low thermal conductivity comparing with the steel tube, the heat flux decreases with time at the deposit layer. As a result, the deposit surface temperature increases. At the region without deposit formation, both the heat flux and surface temperature remain

---

[5] Note: K_A = 1 if deposition forms at both the windward and leeward sections of tube.

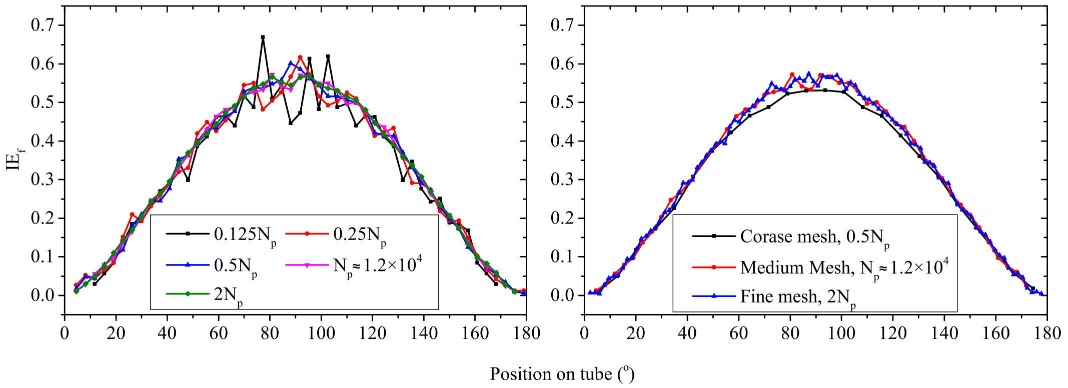

Fig. 5. Independence study of the baseline test.

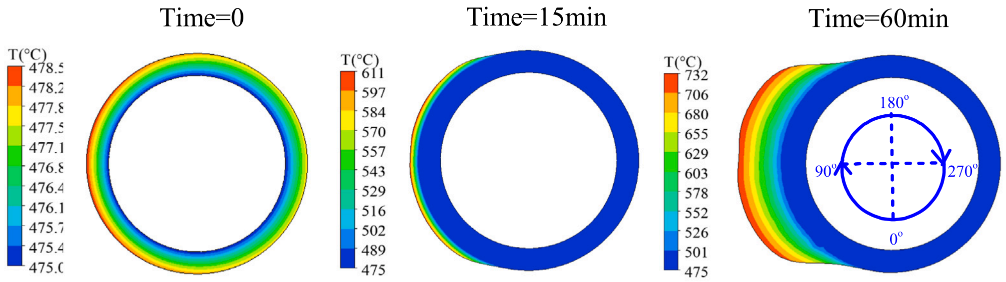

(a) Temperature contour of the solid zone (deposit+steel tube)

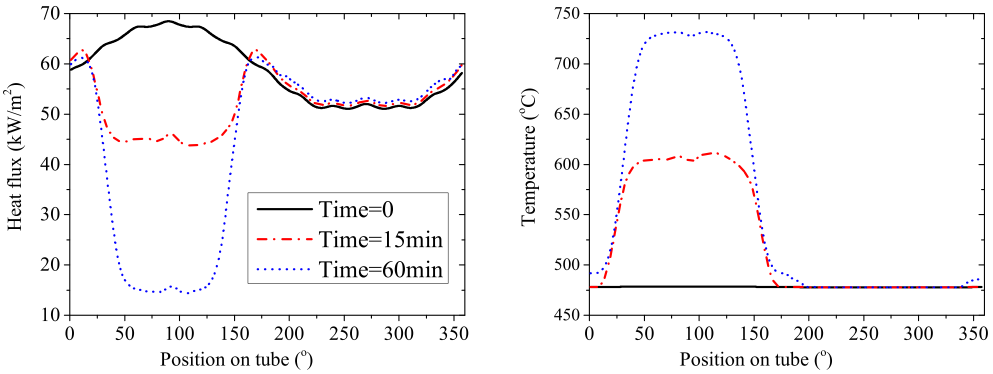

(b) Heat flux of the deposit surface exposed to flue gas

(c) Deposit surface temperature exposed to flue gas

Fig. 6. Temperature contour of the solid zone, heat flux and temperature of the deposit surface for deposition time of 0, 15 and 60 min.

essentially unchanged. The heat flux at the position of 90° decreases from 68 $\mathrm{kW/m^2}$ to 46 and 16 $\mathrm{kW/m^2}$ at the time of 15 and 60 min. Correspondingly, the temperature at the same location increases by 124 and 248 °C and the overall heat transfer (integration of heat flux over the tube surface) drops by 9.4% and 21.0% at the same times respectively.

4.1.2. Overall sticking, erosion and deposition efficiency

Fig. 7 shows the predicted overall sticking efficiency ($\eta_{s,o}$), erosion efficiency ($\eta_{e,o}$) and deposition efficiency ($\eta_{dep,o}$) as a function of deposition time.[6] The sticking efficiency increases from approximately 9.4% to 11.2%, 12.4%, and 13.7% at the time of 15 min, 30 min and 60 min respectively. The erosion efficiency reduces from approximately 1.8% to 1.4%, 1.2% and 1.1% at the same time points respectively. This indicates that the ratio of erosion mass to sticking mass changes from 19.1% to 12.5%, 9.7% and 8.0%. Correspondingly, the overall deposition efficiency increases from approximately 3.7% to 4.8%, 5.4% and 5.9% at the three time points respectively. The increase rate in the deposition rate, which is defined as the ratio of the change in the overall deposition efficiency to deposition time, gradually decreases. The increase rate in the first 15 min (0–15 min), = 7×10^{-4} /min, is approximately twice of that in the second 15 min (15–30 min), = 3.9×10^{-4} /min, which is also approximately twice of that in the second 30 min (30–60 min), = 1.9×10^{-4} /min.

Fig. 8 shows the overall particle deposition efficiency as a function of particle size under the three deposition times. The efficiency firstly increases with particle size and then it reduces with particle size. This trend is due to the effect of particle size on particle impaction efficiency and net sticking efficiency. Increasing particle size increases particle Stokes number, which enhances the potential of particle impaction.

---

[6] Note: $\eta_{s,o}$ is defined by the ratio of the sticking mass to the arrival mass at a time step, $= \frac{\sum_{i=1}^{n}(R_{dep}A_{p,i})}{\sum_{i=1}^{n}(A_{arrival}A_{p,i})}$; $\eta_{e,o}$ is defined by the ratio of the erosion mass to the arrival mass at a time step, $= \frac{\sum_{i=1}^{n}(A_{arrival}(1-\eta_s)\eta_e A_{p,i})}{\sum_{i=1}^{n}(A_{arrival}A_{p,i})}$; $\eta_{dep,o}$ is defined by the ratio of the deposition mass to the inject ash mass at the projected inlet from the tube at a time step, $= \frac{\sum_{i=1}^{n}(R_{dep}A_{p,i})}{F_{par}*L_{proj}}$; where, $A_{p,i}$ is the area of a local face grid of deposition probe.

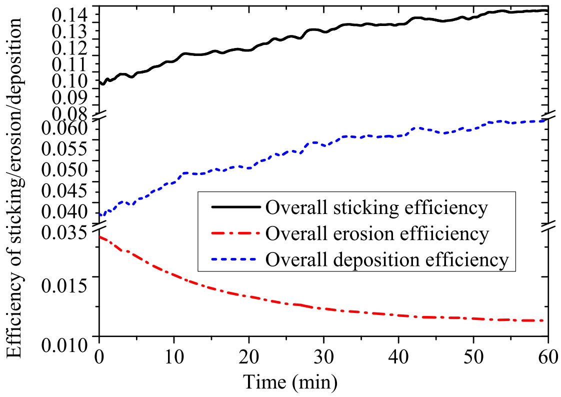

Fig. 7. The overall sticking efficiency, erosion efficiency and deposition efficiency as a function of deposition time.

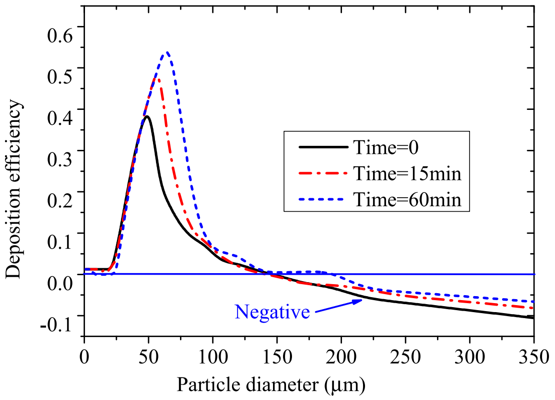

Fig. 8. The overall particle deposition efficiency as a function of particle size for deposition time of 0, 15 and 60 min.

The potential of particle sticking reduces with particle size and particle erosion increases with particles size. As a result, particle net sticking efficiency reduces with particle size. Therefore, there is a maximum deposition efficiency as shown in Fig. 8. Yang et al. [37] numerically observed a similar relationship between the deposition efficiency and particle size. Particle diameter at the maximum deposition efficiency changed from 100 μm to 30 μm with increasing flue gas velocity from 0.36 m/s to 5 m/s. In this study, particle diameter of the maximum deposition efficiency ranges from 50–70 μm at the flue gas velocity of 1 m/s, which is comparable to the previous study. It is also observed that the particle deposition efficiency increases with deposition time. The maximum deposition efficiency increases from approximately 40% to 52% and 57% with the deposition time moving to 15 min and 60 min. This is because the increase in the deposit surface temperature with deposition time as presented in Fig. 6. Interestingly, it is observed that particle deposition efficiency is negative when particle size approximately > 150–200 μm and the efficiency further reduces to approximately [−7%, −11%] when particle size = 350 μm. This suggests that the coarse particles contribute to reducing deposit formation. However, only using particle sticking based deposition model cannot capture this behaviour.

4.2. Influence of operation conditions on deposition

Fig. 9(a)[7] shows the effect of flue gas temperature on ash deposition. Deposit formation rate increases with the temperature. This is explained by the effect of the temperature on particle sticking and erosion behaviour. Increasing the temperature decreases the Young's modulus of the particles and deposit surface. This results in the increase of particle sticking efficiency. Particle erosion also reduces with the temperature according to Eq. (5) of the erosion model. The prediction, ranging from approximately 90 to 1520 $\text{g}/(\text{m}^2\ \text{h})$, adequately matches with the measurement, ranging from approximately 210 to 1370 $\text{g}/(\text{m}^2\ \text{h})$, with increasing the temperature from 589 °C to 968 °C.

Fig. 9(b) shows the effect of tube surface temperature on ash deposition. Experimental deposit formation rate is positively correlated with tube surface temperature. This trend is also observed in the prediction using the CFD based deposition model. The predicted rate, ranging from 300 to 650 $\text{g}/(\text{m}^2\ \text{h})$, is comparable to the measurement, ranging from 40 to 640 $\text{g}/(\text{m}^2\ \text{h})$, with increasing the temperature from 300 to 550 °C. However, the prediction using the mechanistic model, which presents a negative correlation between the deposition rate and tube surface temperature, is opposite to the experimental trend. This is due to that increasing tube surface temperature can reduce the temperature gradient around the deposition surface. This leads to the decrease in the thermophoretic deposition predicted by the mechanistic model [19]. However, the erosion model in the CFD cases predicts less erosion with increasing deposit surface temperature according to Eq. (5). This leads to the increase in the CFD predicted deposit formation rate even though the CFD model also predicts a reduce in the deposit formation rate contributed by thermophoresis, which reduces from approximately 60 to 30 $\text{g}/(\text{m}^2\ \text{h})$ with increasing the temperature from 300 to 550 °C.

Fig. 9(c) shows the effect of flue gas velocity on ash deposition. Deposit formation rate reduces with increasing the velocity for both flue gas temperatures of 781 °C and 968 °C. At the temperature of 781 °C, the prediction using the CFD based model, ranging from 860 to 10 $\text{g}/(\text{m}^2\ \text{h})$, agrees well with the measurement, ranging from 720 to 50 $\text{g}/(\text{m}^2\ \text{h})$, with increasing the velocity from 0.7 to 3.0 m/s. However, the prediction using the mechanistic model, ranging from 580 to 250 $\text{g}/(\text{m}^2\ \text{h})$, cannot accurately capture the significant reduce in the experimental rate, ranging from 640 to 50 $\text{g}/(\text{m}^2\ \text{h})$, with the velocity increasing from 1 to 3.0 m/s. At the temperature of 968 °C, both predictions from the two models cannot accurately capture the relatively small reduce in the rate with increasing velocity from 1.0 to 3.0 m/s. The CFD based model under-predicts the rate by approximately 300 to 400 $\text{g}/(\text{m}^2\ \text{h})$ than the measurement at higher velocities of 3.25 and 3.5 m/s. The temperature of 968 °C is in the ranges of hemispherical temperature and flow temperature of $K_2Si_4O_9$ (852 °C and 1142 °C [31]). This indicates that the ash particles may be highly melted. However, the sticking model used in both ash deposition models is based on the assumption of elastic–plastic particle collision, which may be less accurate at the condition when a particle is highly melted. A more robust sticking model that can cover a larger temperature range of $K_2Si_4O_9$ particles is required, which is considered to be a future work. It is noticed that the prediction using the mechanistic model drops slower than the CFD based prediction at both flue gas temperatures. This may be because that the thermophoretic deposition is empirically estimated from the thermophoretic velocity in the mechanistic model. However, in the CFD based model, the thermophoretic deposition is directly resolved by adding the thermophoretic force into particle motion equations. This may result in a higher decrease in the deposition rate with increasing the velocity in the CFD based model.

Fig. 9(d) shows the effect of ash flux on ash deposition. The predicted deposition rate using both models increases with ash flux and

---

[7] Note: The results of the mechanistic model are from [19]. The results are used for comparing with those using the CFD based deposition model proposed in this study in order to better understand the performance of each models.

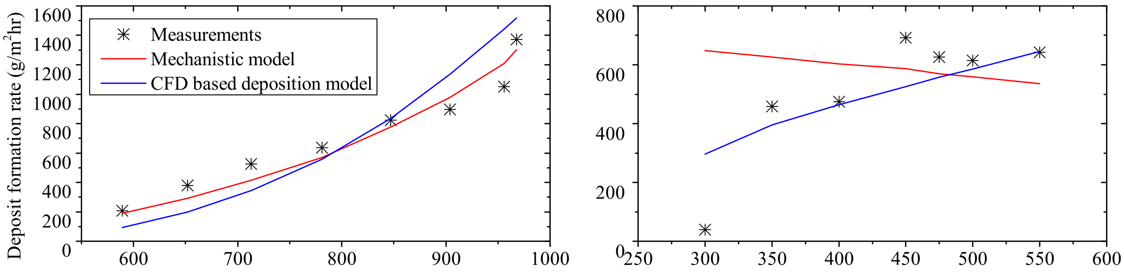

(a) Flue gas temperature (°C)

(b) Tube surface temperature (°C)

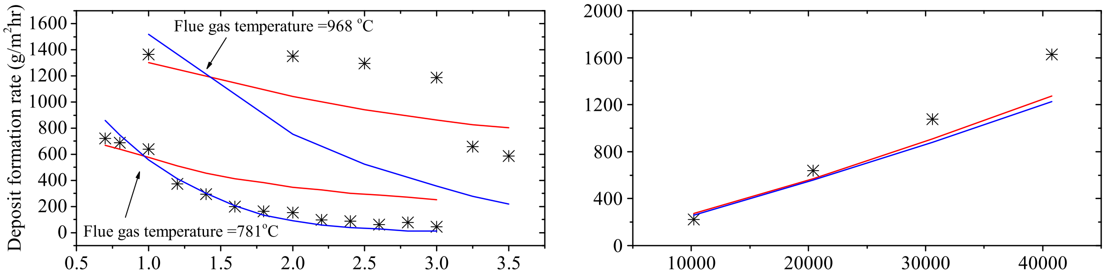

(c) Flue gas velocity (m/s)

(d) Fly ash flux (g/m^{2}hr)

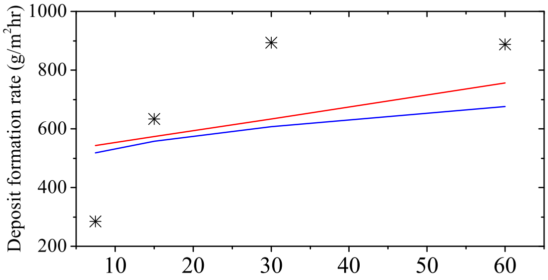

(e) Deposition time (min)

Fig. 9. The effect of operation conditions on deposition: (a) flue gas temperature; (b) tube surface temperature; (c) flue gas velocity; (d) fly ash flux; (e) deposition time.

this observation is consistent with the measurement. However, the deviations between the prediction and the measurement gradually increase from approximately 40 to 400 g/(m^2 h) with increasing ash flux from 10 200 to 40 800 g/(m^2 h). This may be due to the enhanced contribution of deposit surface on deposition with an increased ash flux. Fig. 9(e) shows the effect of deposition time on deposit formation rate. The measured rate increases from approximately 300 to 900 g/(m^2 h) within the first half hour and then keep essentially unchanged in the second half hour. Although the two models predict the increase in the rate with increasing time, the predicted rate only increases from approximately 500 to 600 g/(m^2 h) with increasing time from 7.5 to 30 min and the predicted rate is approximately 300 g/(m^2 h) smaller than the measurements at 30 min. This highlights the important contribution of deposit surface to the deposit formation. The deviation suggests the ash deposition models may underestimate the contribution of the deposit surface, compared with the measurement. In both the mechanistic and CFD based models, the contribution of deposit layer is considered through using the effective Young's modulus, $E^{\star}$, which is based on the Young's modulus of impaction particles (E_p) and deposit surface (E_{surf}) according to Eq. (D.3). Similar consideration of the effective Young's modulus is also observed in the Refs. [20,32,38]. At the initial stage of deposition, deposit surface temperature is much smaller than particle temperature. Correspondingly, E_p is much smaller than E_{surf} as indicated by $\frac{E_p}{E_{surf}} = e^{(-1.155\times10^{-2}(T_p-T_{surf}))}$ (≈0.03 if T_p=781 °C and T_{surf}=475 °C) from Eq. (2) and therefore $E^{\star}$ is mainly dictated by E_p from Eq. (D.3). This leads to the relatively smaller contribution of deposit layer on deposition than the experimental observation.

4.3. Remarks on particle erosion

In this paper, the empirical particle erosion model proposed by Libertowski et al. [21] is implemented and extended for considering different flue gas temperatures and tube surface temperatures. Comparing with the experimental results in the deposit formation rate, the ash deposition model considering particle erosion is able to perform well. This is also observed in the performance of the ash deposition models taking into account particle erosion developed by other previous studies [15–18]. Considering particle erosion is attractive for predicting ash deposition as coarse particles are able to reduce the deposition formation from fine-medium particles as shown in Fig. 8. This is important to understand the mechanisms of using additives with high melting points to control ash deposit formation. Fig. 10 shows the predicted erosion rate[8] is essentially negatively correlated with the experimental deposit formation rate for the 37 deposition cases investigated. This should be reasonable as a deposition test at the condition with a high flue gas velocity and low temperature often presents a low deposition rate and a high erosion rate. The predicted erosion rate is higher at the lower measured deposition rate (<100 g/(m^2 h)), as shown by the blue triangle points in Fig. 10. At the region of higher experimental deposition rate (>800 g/(m^2 h)), the predicted erosion rate is well below 100 g/(m^2 h). However, it should be noticed

---

[8] Note: Erosion rate is defined as the accumulation of mass flux according to the erosion term in Eq. (1) over the deposition time. Deposit formation rate is based on particle sticking and erosion behaviours.

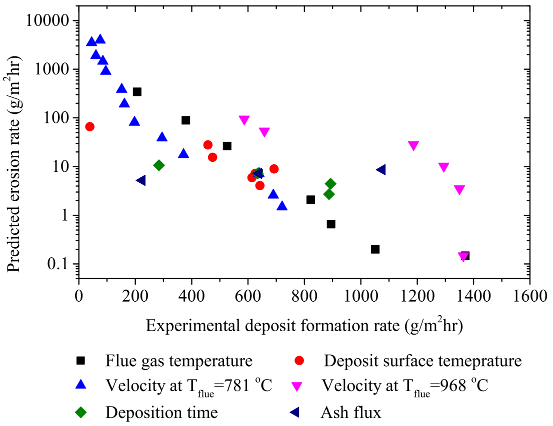

Fig. 10. The predicted erosion rate as a function of the experimental deposit formation rate for all the 37 deposition cases. (For interpretation of the references to colour in this figure legend, the reader is referred to the web version of this article.)

that the erosion model is validated against the overall experimental deposition observations. Further ash deposition tests, which are able to separate erosion behaviour from sticking behaviour, are needed to improve the prediction and understanding the contribution of particle erosion in ash deposition.

5. Conclusions

1. A dynamic CFD based ash deposition model with conjugate heat transfer is developed for the modelling of ash deposition of a model biomass fly ash species ($K_2Si_4O_9$) in a lab-scale entrained flow reactor under multiple operation conditions. A globally mass-conserving smooth method is proposed through a multiple-point weighted moving average algorithm and a growth scaling factor. A new method to estimate particle count for Lagrangian particle tracking is also proposed, which is based on particle impaction efficiency and face count of the tube surface. By using the proposed smooth method with the setting of five point and the estimated particle count, a stable dynamic mesh morphing can be achieved for all the 37 deposition cases investigated without either looping the smooth process or sub-grouping/averaging the thickness growth.
2. An expression of Young's modulus of $K_2Si_4O_9$ particles and deposits versus temperature has been developed for the two body collision model in order to predict particle sticking efficiency at the conditions of varied temperatures. The empirical erosion model is also extended for considering particle temperature and deposit surface temperature. The prediction results using the proposed ash deposition model agrees reasonably with the experimental observation of the effects of flue gas temperature, tube surface temperature, flue gas velocity, fly ash flux and deposition time on deposit formation. R^2 of the predicted and measured deposit formation rates is approximately 0.68. However, it is still noticed that there are as much as 200–300 g/(m^2 h) over-predictions of the deposit formation rate for the cases at the relatively low tube surface temperature and at the beginning of ash deposition. This may be due to the underestimation of the contribution of deposited surface to deposition.
3. The predicted erosion rate is observed to be correlated negatively with the experimental deposition rate. Taking into account particle erosion is attractive as the model can consider the contribution of coarse particle to reduce the deposit formation from smaller particles.

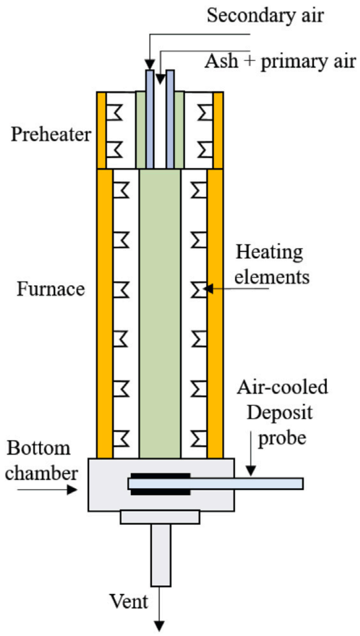

Fig. A.11. Schematic diagram of the EFR.
Source: Modified from [19].

CRediT authorship contribution statement

Xin Yang: Conceptualization, Methodology, Software, Validation, Investigation, Data curation, Writing – original draft, Writing – review & editing, Visualization, Project administration, Funding acquisition. **Hao Zhou:** Conceptualization, Writing – review & editing, Project administration, Funding acquisition. **Hao Wu:** Experimental data, Writing – review & editing.

Declaration of competing interest

The authors declare that they have no known competing financial interests or personal relationships that could have appeared to influence the work reported in this paper.

Acknowledgements

The authors would like to acknowledge State Key Laboratory of Clean Energy Utilization, China and Zhejiang University, China for funding the project (grant number CEU2020016).

Appendix A. Schematic diagram of the EFR

See Fig. A.11.

Appendix B. Operation conditions

See Table B.1.

Appendix C. Particle size distribution

See Fig. C.12.

Table B.1
Operating conditions of the tests: the symbol next to test number, ⋆, represents the test case used as the training data.

No.	T_g, °C	T_t, °C	V_g, m/s	T_{dep}, min	F_{par}, g/(m^2 h)
1⋆	589	475	1.0	15	2.04×10^4
2	652	475	1.0	15	2.04×10^4
3	713	475	1.0	15	2.04×10^4
4⋆	781	475	1.0	15	2.04×10^4
5	847	475	1.0	15	2.04×10^4
6	904	475	1.0	15	2.04×10^4
7	956	475	1.0	15	2.04×10^4
8⋆	968	475	1.0	15	2.04×10^4
9⋆	781	300	1.0	15	2.04×10^4
10	781	350	1.0	15	2.04×10^4
11	781	400	1.0	15	2.04×10^4
12	781	450	1.0	15	2.04×10^4
13	781	500	1.0	15	2.04×10^4
14⋆	781	550	1.0	15	2.04×10^4
15⋆	781	475	0.7	15	2.04×10^4
16	781	475	0.8	15	2.04×10^4
17	781	475	1.2	15	2.04×10^4
18	781	475	1.4	15	2.04×10^4
19	781	475	1.6	15	2.04×10^4
20	781	475	1.8	15	2.04×10^4
21	781	475	2.0	15	2.04×10^4
22	781	475	2.2	15	2.04×10^4
23	781	475	2.4	15	2.04×10^4
24	781	475	2.6	15	2.04×10^4
25	781	475	2.8	15	2.04×10^4
26⋆	781	475	3.0	15	2.04×10^4
27	968	475	2.0	15	2.04×10^4
28	968	475	2.5	15	2.04×10^4
29	968	475	3	15	2.04×10^4
30	968	475	3.25	15	2.04×10^4
31⋆	968	475	3.5	15	2.04×10^4
32	781	475	1.0	7.5	2.04×10^4
33	781	475	1.0	30	2.04×10^4
34	781	475	1.0	60	2.04×10^4
35	781	475	1.0	15	1.02×10^4
36	781	475	1.0	15	3.06×10^4
37	781	475	1.0	15	4.08×10^4

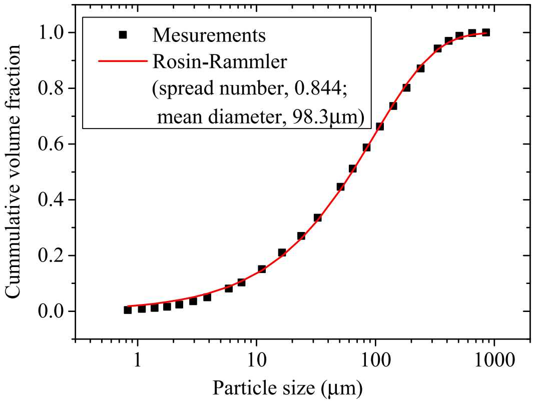

Fig. C.12. Particle size distribution of $K_2Si_4O_9$ used in the tests.

Appendix D. Sticking efficiency

There are four steps to implement the two body collision based sticking model: (i) Step 1: calculate the critical particle impaction angle, θ_{cr}; (ii) Step 2: calculate the critical normal impaction velocity, V_{cr}; (iii) Step 3: energy conservation analysis; and (iv) Step 4: calculate sticking efficiency and particle rebound velocities.

Step 1→ θ_{cr}:

$$\theta_{cr} = \frac{f}{\sqrt{32\beta^3}}\sqrt{\frac{2(2-\nu)}{(1-\nu)}} \tag{D.1}$$

where f is the friction coefficient; β is the fraction of contact radius; ν is Poisson's ratio.

Step 2→ V_{cr}:

$$V_{cr} = \frac{\pi^2}{2\sqrt{10\rho_p}}\frac{(1.59Y)^{5/2}}{E^{\star 2}}\left(\frac{r_0}{1+r_0}\right)^{(3/2)}\sqrt{\frac{1+C_m}{C_m}} \tag{D.2}$$

$$\frac{1}{E^\star} = \frac{1-\nu^2}{E_p} + \frac{1-\nu^2}{E_{surf}} \tag{D.3}$$

where ρ_p is the particle density, Y is the uniaxial yield stress of particles, r_0 is the radius ratio, C_m is the mass ratio; E_p is the Young's modulus of particles. E_{surf} is the Young's modulus of deposit and steel, respectively. If the Young's modulus of deposit is used, the sticking efficiency predicted is $\eta_{s,dep}$ presented in Eq. (4); if the Young's modulus of steel (E_{steel}) is used, the sticking efficiency predicted is $\eta_{s,steel}$ presented in Eq. (4). The Young's modulus of particles and deposit is predicted using Eq. (2). The Young's modulus of steel is estimated by [39]:

$$E_{steel} = (-0.072T + 220.47)\times 10^9 \tag{D.4}$$

Step 3.1→ elastic impact when $\theta_I < \theta_{cr}$ and $V_{in} <= V_{cr}$:

$$R^\star = \frac{1}{2}D_p\frac{r_0}{(1+r_0)} \tag{D.5}$$

$$R_c = R^\star \tag{D.6}$$

$$Q_p = 0 \tag{D.7}$$

$$\Delta Q = 7.09\left(\frac{R_c^4 W_A^5}{E^{\star 2}}\right)^{1/3} \tag{D.8}$$

where V_{in} is the particle impact velocity normal to local tube surface, D_p is the particle diameter, m_p is the particle mass, and W_A is the work of adhesion.

Step 3.2→ elastic–plastic impact when $\theta_I < \theta_{cr}$ and $V_{in} > V_{cr}$:

$$m^\star = m_p \frac{C_m}{1+C_m} \tag{D.9}$$

$$h_{el} = \left(\frac{2}{3}\pi\right)^2 \frac{R^\star}{(4/3E^\star)^2}(1.59Y)^2 \tag{D.10}$$

$$Q_{el} = \frac{2}{5}\left(\frac{2}{3}\pi\right)^5 \frac{R^{\star 3}}{(4/3E^\star)^4}(1.59Y)^5 \tag{D.11}$$

$$Q_k = \frac{1}{2} m^\star V_{in}^2 \tag{D.12}$$

$$r_{el} = \frac{\pi R^\star}{2E^\star}(1.59Y) \tag{D.13}$$

$$K_a = \frac{1}{4\pi R^\star (1.59Y)} \tag{D.14}$$

$$K_b = \frac{1}{2} h_{el} - W_A/(1.59Y) \tag{D.15}$$

$$K_c = Q_{el} - Q_k - \pi W_A r_{el}^2 \tag{D.16}$$

$$\Delta F = \frac{(-K_b + \sqrt{K_b^2 - 4K_a K_c})}{2K_a} \tag{D.17}$$

$$Q_p = \frac{\Delta F^2}{4\pi R^\star (1.59Y)} \tag{D.18}$$

$$r_t = \sqrt{r_{el}^2 + \frac{\Delta F}{\pi(1.59Y)}} \tag{D.19}$$

$$F_{el} = \left(\frac{2}{3}\pi\right)^3 \frac{R^{\star 2}}{(4/3E^\star)^2}(1.59Y)^3 \tag{D.20}$$

$$F = \Delta F + F_{el} \tag{D.21}$$

$$R_c = \frac{3/4E^\star r_t^3}{F} \tag{D.22}$$

$$\Delta Q = 7.09\left(\frac{R_c^4 W_A^5}{E^{\star 2}}\right)^{1/3} \tag{D.23}$$

Step 3.3→ $Ex_E^\star$:

$$Ex_E^\star = 1 - \frac{Q_p + \Delta Q}{\frac{1}{2} m^\star V_{in}^2} \tag{D.24}$$

Step 4.1→ η_s, V_{rn}, and V_{rt} for $\theta_I < \theta_{cr}$ and $Ex_E^\star \leq 0$:

$$\eta_s = 1 \tag{D.25}$$

$$V_{rn} = 0 \tag{D.26}$$

$$V_{rt} = 0 \tag{D.27}$$

Step 4.2→ η_s, V_{rn}, and V_{rt} for $\theta_I < \theta_{cr}$ and $Ex_E^\star > 0$:

$$\eta_s = 0 \tag{D.28}$$

$$cor_r = \sqrt{Ex_E^\star} \tag{D.29}$$

$$V_{rn} = cor_r V_{in} \tag{D.30}$$

$$cr_r = f - \frac{2}{7}\frac{\tan\theta_I}{(1+cor_r)} \tag{D.31}$$

Table D.2
Parameters used in the model.

Parameters	Values
Friction coefficient, f	0.7
Poisson's ratio, ν	0.3
Uniaxial yield stress of particles, Y, Pa	4.1×10^8
Radius ratio, r_0	1
Mass ratio, C_m	2
The work of adhesion, W_A, J/m^2	0.3
Fraction of contact radius, β	0.128
Constant, b_1	1.1918
Constant, b_2	1

$$V_{rt} = \begin{cases} V_{it}\left(1 - \frac{2}{7}\frac{C_m}{1+C_m}\right) & cr_r > 0 \\ V_{it}\left(1 - \frac{f(1+cor_r)}{\tan\theta_I}\frac{C_m}{1+C_m}\right) & cr_r \leq 0 \end{cases} \tag{D.32}$$

Step 4.3→ η_s, V_{rn}, and V_{rt} for $\theta_I \geq \theta_{cr}$:

$$\eta_s = 0 \tag{D.33}$$

$$V_r = \sqrt{V_I^2\left(1 - b_1(\frac{1}{2}\pi - \theta_I)\right)} \tag{D.34}$$

$$V_{rn} = V_{in}\max(0.75, b_2\theta_I - 1.2) \tag{D.35}$$

$$V_{rt} = \sqrt{V_r^2 - V_{rn}^2} \tag{D.36}$$

where b_1 and b_2 are empirical constants.

Table D.2 lists the values of the parameters used in the model. The values of f, ν, Y, r_0, C_m, W_A are from van Beek [20]; the value of β is estimated from Zheng et al. [18]; the values of b_1 and b_2 are from Zheng et al. [18].

Appendix E. Properties of $K_2Si_4O_9$ particle, air and steel

See Table E.3.

Appendix F. Further analysis using liquid phase dependent porosity model

The deposit surface temperatures of cases (6,7,8,27,28, and 34) are above the deformation temperature. This only happens at the later stage of deposition time even though the temperatures are still well below the hemispherical temperature. In order to clarify the uncertainty of using constant porosity for these six cases, further calculations are carried out through adding the liquid phase dependent porosity model presented by Richards et al. [34] into the dynamic ash deposition model. In addition, due to the limited data of the melting behaviour (ash liquid volume fraction) as a function of temperature for $K_2Si_4O_9$, it is assumed that: the liquid volume fraction is linearly dependent with temperature; the volume fraction equals to zero at the deformation temperature and it increases to unity at the hemispherical temperature. Therefore, the porosity is predicted by:

$$\phi = 1 - \left((1-\phi_0) + \frac{R_{melt}}{1-R_{melt}}(1-\phi_0)\right) \tag{F.1}$$

$$R_{melt} = 0.00704T - 6.92 \tag{F.2}$$

where, ϕ_0 is the initial porosity, =0.6; R_{melt} is the liquid volume fraction; T is temperature. The predicted deposition formation rates using constant porosity and R_{melt} dependent porosity are presented in Table F.4. It is seen that the predicted deposit formation rate using R_{melt} dependent porosity is slightly smaller than that using constant porosity. This is because the reduced porosity at the later stage of deposition time increases the thermal conductivity of deposit. The difference in the predicted deposit formation rate between constant porosity and

Table E.3
Properties of $K_2Si_4O_9$ particle, air and steel.

Material	Parameters	Values/correlations	Source
Particle	Density, ρ_p, kg/m^3	2400	[40]
	Heat capacity, c_p, J/(kgK)	$450.6 - 0.1161T - 1.67 \times 10^7 T^{-2}$	[41]
	Heat conductivity, k_p, W/(mK)	$0.0015T^{1.1}$	[42]
	Emissivity, ξ_p	$0.3\log_{10}(D_p \times 10^6) + 0.16$	[43]
Air	Heat conductivity, k_g, W/(mK)	$0.03994\left(\frac{T}{500}\right)^{0.77}$	[44]
Steel	Heat conductivity, k_{steel}, W/(mK)	21.5	[45]

Table F.4
Predicted deposit formation rate (g/(m^2 h)) using constant porosity and R_{melt} dependent porosity.

	Case 6	Case 7	Case 8	Case 27	Case 28	Case 34
Constant porosity	1135.4	1443.2	1519.2	753.6	524.7	675.7
Non-constant porosity	1131.5	1425.6	1488.4	749.5	522.7	675.3

R_{melt} dependent porosity is within approximately 2%. Therefore, the assumption in constant porosity should be acceptable in this study.

References

[1] Finney KN, Akram M, Diego ME, Yang X, Pourkashanian M. Chapter 2 - carbon capture technologies. In: Magalhães Pires JC, Cunha Gonçalves ALD, editors. Bioenergy with carbon capture and storage. Academic Press; 2019, p. 15–45. http://dx.doi.org/10.1016/B978-0-12-816229-3.00002-8.

[2] Jia Z, Lin B. How to achieve the first step of the carbon-neutrality 2060 target in China: The coal substitution perspective. Energy 2021;233:121179. http://dx.doi.org/10.1016/j.energy.2021.121179.

[3] Hupa M, Karlström O, Vainio E. Biomass combustion technology development – It is all about chemical details. Proc Combust Inst 2017;36(1):113–34. http://dx.doi.org/10.1016/j.proci.2016.06.152.

[4] Wang Y, Tan H, Wang X, Cao R, Wei B. The condensation and thermodynamic characteristics of alkali compound vapors on wall during wheat straw combustion. Fuel 2017;187:33–42. http://dx.doi.org/10.1016/j.fuel.2016.09.014.

[5] Mueller C, Selenius M, Theis M, Skrifvars B-J, Backman R, et al. Deposition behaviour of molten alkali-rich fly ashes—development of a submodel for CFD applications. Proc Combust Inst 2005;30(2):2991–8. http://dx.doi.org/10.1016/j.proci.2004.08.116.

[6] Kær S, Rosendahl L, Baxter L. Towards a CFD-based mechanistic deposit formation model for straw-fired boilers. Fuel 2006;85(5):833–48. http://dx.doi.org/10.1016/j.fuel.2005.08.016.

[7] Chapela S, Porteiro J, Gómez M, Patiño D, Míguez J. Comprehensive CFD modeling of the ash deposition in a biomass packed bed burner. Fuel 2018;234:1099–122. http://dx.doi.org/10.1016/j.fuel.2018.07.121.

[8] Chapela S, Cid N, Porteiro J, Míguez JL. Numerical transient modelling of the fouling phenomena and its influence on thermal performance in a low-scale biomass shell boiler. Renew Energy 2020;161:309–18. http://dx.doi.org/10.1016/j.renene.2020.07.068.

[9] Yang X, Ingham D, Ma L, Zhou H, Pourkashanian M. Understanding the ash deposition formation in zhundong lignite combustion through dynamic CFD modelling analysis. Fuel 2017;194:533–43. http://dx.doi.org/10.1016/j.fuel.2017.01.026.

[10] García Pérez M, Vakkilainen E, Hyppänen T. Fouling growth modeling of kraft recovery boiler fume ash deposits with dynamic meshes and a mechanistic sticking approach. Fuel 2016;185:872–85. http://dx.doi.org/10.1016/j.fuel.2016.08.045.

[11] Tang S-Z, He Y-L, Wang F-L, Tao Y-B. Parametric study on fouling mechanism and heat transfer characteristics of tube bundle heat exchangers for reducing fouling considering the deposition and removal mechanisms. Fuel 2018;211:301–11. http://dx.doi.org/10.1016/j.fuel.2017.09.015.

[12] Mu L, Miao H, Zhao C, Zhai Z, Shang Y, Yin H. Dynamic CFD modeling evaluation of ash deposition behavior and morphology evolution with different tube arrangements. Powder Technol 2021;379:279–95. http://dx.doi.org/10.1016/j.powtec.2020.10.057.

[13] Zheng Z, Yang W, Yu P, Cai Y, Zhou H, Boon SK, et al. Simulating growth of ash deposit in boiler heat exchanger tube based on CFD dynamic mesh technique. Fuel 2020;259:116083. http://dx.doi.org/10.1016/j.fuel.2019.116083.

[14] Zhou H, Zhang K, Li Y, Zhang J, Zhou M. Simulation of ash deposition in different furnace temperature with a 2d dynamic mesh model. J Energy Inst 2019;92(6):1743–56. http://dx.doi.org/10.1016/j.joei.2018.12.006.

[15] Strandström K, Mueller C, Hupa M. Development of an ash particle deposition model considering build-up and removal mechanisms. Fuel Process Technol 2007;88(11):1053–60. http://dx.doi.org/10.1016/j.fuproc.2007.06.024, Impacts of Fuel Quality on Power Production.

[16] Liu C, Liu Z, Zhang T, Huang X, Guo J, Zheng C. Numerical investigation on development of initial ash deposition layer for a high-alkali coal. Energy Fuels 2017;31(3):2596–606. http://dx.doi.org/10.1021/acs.energyfuels.6b03043.

[17] Zhou H, Hu S. Numerical simulation of ash deposition behavior with a novel erosion model using dynamic mesh. Fuel 2021;286:119482. http://dx.doi.org/10.1016/j.fuel.2020.119482.

[18] Zheng Z, Yang W, Wang H, Zhou A, Cai Y, Zeng G, et al. Development of a mechanistic fouling model for predicting deposit formation in a woodchip-fired grate boiler. Energy 2021;220:119699. http://dx.doi.org/10.1016/j.energy.2020.119699.

[19] Laxminarayan Y, Jensen PA, Wu H, Frandsen FJ, Sander B, Glarborg P. Biomass fly ash deposition in an entrained flow reactor. Proc Combust Inst 2019;37(3):2689–96. http://dx.doi.org/10.1016/j.proci.2018.06.039.

[20] Van Beek MC. Gas-side fouling of heat recovery boilers [Ph.D. thesis], Technische Universiteit Eindhoven; 2001.

[21] Libertowski ND, Geiger GM, Bons JP. Modeling deposit erosion in internal turbine cooling geometries. J Eng Gas Turbines Power 2020;142(3). http://dx.doi.org/10.1115/1.4045954.

[22] Wu H, Bashir MS, Jensen PA, Sander B, Glarborg P. Impact of coal fly ash addition on ash transformation and deposition in a full-scale wood suspension-firing boiler. Fuel 2013;113:632–43. http://dx.doi.org/10.1016/j.fuel.2013.06.018.

[23] Nordgren D, Hedman H, Padban N, Boström D, Öhman M. Ash transformations in pulverised fuel co-combustion of straw and woody biomass. Fuel Process Technol 2013;105:52–8. http://dx.doi.org/10.1016/j.fuproc.2011.05.027, Impacts of Fuel Quality on Power Production and Environment.

[24] Jensen PA, Frandsen FJ, Hansen J, Dam-Johansen K, Henriksen N, Hörlyck S. SEM investigation of superheater deposits from biomass-fired boilers. Energy Fuels 2004;18(2):378–84. http://dx.doi.org/10.1021/ef030097l.

[25] Beckmann A, Mancini M, Weber R, Seebold S, Müller M. Measurements and CFD modeling of a pulverized coal flame with emphasis on ash deposition. Fuel 2016;167:168–79. http://dx.doi.org/10.1016/j.fuel.2015.11.043.

[26] Krishnamoorthy G, Kuznia ME, Smith KM, Seames WS, Wang Y, Wendt JO. Aerodynamic effects on outer ash deposition rates in second generation atmospheric pressure oxy-coal combustion systems. Fuel 2021;303:121217. http://dx.doi.org/10.1016/j.fuel.2021.121217.

[27] Yang X, Szuhánszki J, Tian Y, Ingham D, Ma L, Pourkashanian M. Understanding the effects of oxyfuel combustion and furnace scale on biomass ash deposition. Fuel 2019;247:36–46. http://dx.doi.org/10.1016/j.fuel.2019.03.031.

[28] Ansys Inc. ANSYS FLUENT 19.2 theory guide. 2018, Ansys Inc.

[29] Kleinhans U, Wieland C, Babat S, Spliethoff H. Large eddy simulation of a particle-laden flow around a cylinder: Importance of thermal boundary layer effects for slagging and fouling. Fuel 2019;241:585–606. http://dx.doi.org/10.1016/j.fuel.2018.12.056.

[30] Rajani B, Kandasamy A, Majumdar S. Numerical simulation of laminar flow past a circular cylinder. Appl Math Model 2009;33(3):1228–47. http://dx.doi.org/10.1016/j.apm.2008.01.017.

[31] Laxminarayan Y. Formation, sintering and removal of biomass ash deposits [Ph.D. thesis], Technical University of Denmark; 2018.

[32] Ai W, Kuhlman JM. Simulation of coal ash particle deposition experiments. Energy Fuels 2011;25(2):708–18. http://dx.doi.org/10.1021/ef101294f.

[33] Konstandopoulos AG. Particle sticking/rebound criteria at oblique impact. J Aerosol Sci 2006;37(3):292–305. http://dx.doi.org/10.1016/j.jaerosci.2005.05.019.

[34] Richards GH, Slater PN, Harb JN. Simulation of ash deposit growth in a pulverized coal-fired pilot scale reactor. Energy Fuels 1993;7(6):774–81. http://dx.doi.org/10.1021/ef00042a012.

[35] Sugawara A, Yoshizawa Y. An investigation on the thermal conductivity of porous materials and its application to porous rook. Aust J Phys 1961;14:469–80. http://dx.doi.org/10.1071/PH610469.

[36] Weber R, Schaffel-Mancini N, Mancini M, Kupka T. Fly ash deposition modelling: Requirements for accurate predictions of particle impaction on tubes using RANS-based computational fluid dynamics. Fuel 2013;108:586–96. http://dx.doi.org/10.1016/j.fuel.2012.11.006.

[37] Yang X, Ingham D, Ma L, Troiano M, Pourkashanian M. Prediction of particle sticking efficiency for fly ash deposition at high temperatures. Proc Combust Inst 2019;37(3):2995–3003. http://dx.doi.org/10.1016/j.proci.2018.06.038.

[38] Barker B, Casaday B, Shankara P, Ameri A, Bons JP. Coal ash deposition on nozzle guide vanes—Part II: Computational modeling. J Turbomach 2012;135(1). http://dx.doi.org/10.1115/1.4006399.

[39] Virgamet. STAINLESS STEEL 306 properties. 2021, https://virgamet.com/1-4361-x1crnisi18154-aisi-306-uns-s30600-grade-f46-z1cns1715-stainless-steel. [Accessed: 21 August 2021].

[40] Santa Cruz Biotechnology. Potassium silicate. 2021, https://www.scbt.com/p/potassium-silicate-anhydrous-1312-76-1. [Accessed: 21 August 2021].

[41] Richet P, Bottinga Y. Heat capacity of liquid silicates: new measurements on NaAlSi3O8 and K2Si4O9. Geochim Cosmochim Acta 1980;44(10):1535–41. http://dx.doi.org/10.1016/0016-7037(80)90117-9.

[42] Rezaei H, Gupta R, Bryant G, Hart J, Liu G, Bailey C, et al. Thermal conductivity of coal ash and slags and models used. Fuel 2000;79(13):1697–710. http://dx.doi.org/10.1016/S0016-2361(00)00033-8.

[43] Boow J, Goard PR. Fireside deposits and their effect on heat transfer in a pulverized-fuel-fired boiler: Partlll.the influence of the physical characteristics of the deposit on its radiant emittance and effective thermal conductance. J Inst Fuel 1969;42:412–9.

[44] Engineering ToolBox. Air - thermal conductivity. 2021, https://www.engineeringtoolbox.com/air-properties-viscosity-conductivity-heat-capacity-d_1509.html. [Accessed: 21 August 2021].

[45] The World Material. Aisi 316 stainless steel properties. 2021, https://www.theworldmaterial.com/aisi-316-ss316-stainless-steel-properties-composition/. [Accessed: 21 August 2021].